EDGE ARTICLE

Check for updates

Amyloid-β peptide 37, 38 and 40 individually and cooperatively inhibit amyloid-β 42 aggregation†

Gabriel A. Braun, ‡[a] Alexander J. Dear, [abcd] Kalyani Sanagavarapu,§[a] Henrik Zetterberg[efgh] and Sara Linse *[a]

The pathology of Alzheimer's disease is connected to the aggregation of β-amyloid (Aβ) peptide, which *in vivo* exists as a number of length-variants. Truncations and extensions are found at both the N- and C-termini, relative to the most commonly studied 40- and 42-residue alloforms. Here, we investigate the aggregation of two physiologically abundant alloforms, $A\beta_{37}$ and $A\beta_{38}$, as pure peptides and in mixtures with $A\beta_{40}$ and $A\beta_{42}$. A variety of molar ratios were applied in quaternary mixtures to investigate whether a certain ratio is maximally inhibiting of the more toxic alloform $A\beta_{42}$. Through kinetic analysis, we show that both $A\beta_{37}$ and $A\beta_{38}$ self-assemble through an autocatalytic secondary nucleation reaction to form fibrillar β-sheet-rich aggregates, albeit on a longer timescale than $A\beta_{40}$ or $A\beta_{42}$. Additionally, we show that the shorter alloforms co-aggregate with $A\beta_{40}$, affecting both the kinetics of aggregation and the resulting fibrillar ultrastructure. In contrast, neither $A\beta_{37}$ nor $A\beta_{38}$ forms co-aggregates with $A\beta_{42}$; however, both short alloforms reduce the rate of $A\beta_{42}$ aggregation in a concentration-dependent manner. Finally, we show that the aggregation of $A\beta_{42}$ is more significantly impeded by a combination of $A\beta_{37}$, $A\beta_{38}$, and $A\beta_{40}$ than by any of these alloforms independently. These results demonstrate that the aggregation of any given Aβ alloform is significantly perturbed by the presence of other alloforms, particularly in heterogeneous mixtures, such as is found in the extracellular fluid of the brain.

Introduction

Alzheimer's disease (AD), a progressive neurodegenerative disease, is the most common cause of dementia worldwide, afflicting nearly 50 million people.[1] Although symptomatic treatments for AD exist, there are currently no available means of slowing or reversing the progression of the disease.[2–4] Recently, the anti-amyloid β (Aβ) antibody aducanumab[5–7] was approved for clinical use by the US Food and Drug Administration (FDA),[8] and other promising antibody candidates are in the pipeline, but their clinical efficacy remains uncertain. This is due, in part, to the fact that the etiology of AD remains poorly understood. The most common theory of the progression of AD is the amyloid cascade hypothesis, which contends that aggregation of amyloid β peptide (Aβ) is the critical pathological event responsible for triggering the onset of the disease, with self-assembly of tau an important second step.[9,10] In particular, dispersed Aβ oligomers, rather than the deposited plaques, are widely understood to be the primary cytotoxic forms of these aggregates,[3,11] although fibrils may still play a significant role, directly[12] or indirectly through generation of toxic oligomers through secondary nucleation.[13,14] While the cascade model has been challenged in recent years,[15–17] it is nevertheless commonly accepted that the aggregation of Aβ plays a critical part in the initiation and progression of AD.[18–20] Understanding the Aβ aggregation process, its underlying microscopic steps, and their connection with toxicity, is essential for the development of effective treatments and better diagnostic tools.[21]

Aβ is produced from the transmembrane amyloid precursor protein (APP). In the so-called amyloidogenic pathway for processing of APP, sequential cleavages of the protein by β- and γ-secretases result in the release of Aβ into the extracellular fluid.[22,23] There is some variability in the cleavage sites by both secretases, leading to the presence of Aβ length-variants, or

[a]Biochemistry and Structural Biology, Lund University, Lund, Sweden. E-mail: sara.linse@biochemistry.lu.se

[b]Department of Cell Biology, Harvard Medical School, Boston, MA, USA

[c]Paulson School of Engineering and Applied Science, Harvard University, Cambridge, MA, USA

[d]Department of Chemistry, University of Cambridge, Cambridge, UK

[e]Department of Psychiatry and Neurochemistry, Institute of Neuroscience and Physiology, The Sahlgrenska Academy at the University of Gothenburg, Mölndal, Sweden

[f]Clinical Neurochemistry Laboratory, Sahlgrenska University Hospital, Mölndal, Sweden

[g]Department of Neurodegenerative Disease, UCL Institute of Neurology, Queen Square, London, UK

[h]UK Dementia Research Institute at UCL, London, UK

† Electronic supplementary information (ESI) available. See DOI: 10.1039/d1sc02990h

‡ Current address: University of California, San Francisco, Program in Chemistry and Chemical Biology, San Francisco, CA, United States.

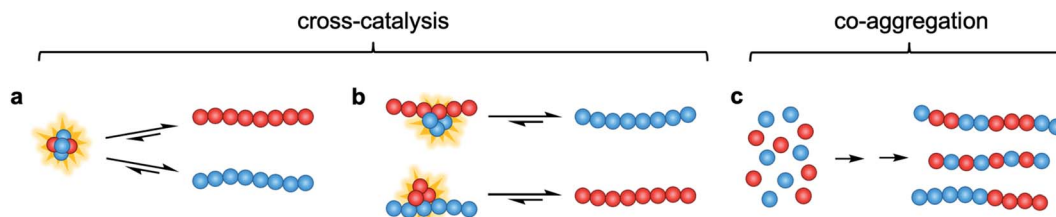§ Current address: Wren Therapeutics Sweden AB, Lund, Sweden.

Fig. 1 Possible modes of cross-catalysis through (a) heterogeneous primary nucleation in co-oligomers or (b) on fibril surfaces. (c) Co-aggregation is here defined as the process leading to any form of aggregates composed of more than one peptide alloform.

alloforms, that are generally between 37 and 43 residues long.[24–27] Of these alloforms, the 40-residue length-variant APP 672-711, $A\beta_{1-40}$, is the predominant form found *in vivo*, making up almost 60% the $A\beta$ peptide present in cerebrospinal fluid (CSF).[28,29] The next most abundant alloforms are $A\beta_{1-38}$, $A\beta_{1-42}$, and $A\beta_{1-37}$, which make up approximately 15%, 10% and 8% of $A\beta$ in CSF, respectively (although the concentration of $A\beta_{1-42}$ in CSF decreases significantly in AD patients, which is proposed to be the result of peptide sequestration in plaques[30,31]). N-terminal length variants are observed both with extended[25] and truncated[32] N-termini, in which case extension retards[33] and truncation accelerates[34] aggregation.

Of the C-terminal $A\beta$ length-variants found most commonly *in vivo*, the 40- and 42-residue alloforms are the most aggregation prone and are also found in the highest abundance in the characteristic AD plaques.[35] As a result, the aggregation of these peptides has been extensively characterized, while the aggregation of shorter, less aggregation-prone alloforms has remained relatively less studied.[36] Using a chemical kinetics approach, the microscopic steps underlying the *in vitro* aggregation of $A\beta$ have previously been identified from global analyses of large sets of data over ranges of peptide concentration,[37,38] showing that $A\beta$ peptides, ending at residue 40 and 42, respectively, aggregate through a nucleation-and-growth pathway in which the formation of new aggregates occurs predominantly through the autocatalytic secondary nucleation on the surface of existing fibrils.[14] However, the aggregation behavior of $A\beta$ peptides is highly sensitive to solution conditions, including ionic strength[39,40] and pH,[41] and to the presence of foreign surfaces, such as phospholipid membranes[42,43] and nanoparticles.[44,45] Indeed, in the complex milieu of cerebrospinal fluid, it has been found that, while $A\beta_{42}$ aggregates through a secondary-nucleation-dominated mechanism, the rate of this fibril-catalyzed nucleation is significantly reduced relative to that of the peptide in pure buffer.[46,47] Additionally, the aggregation of $A\beta$ peptides is perturbed by the co-existence of $A\beta$ peptides of different lengths. For example, it has previously been shown that, while $A\beta_{42}$ and $A\beta_{40}$ aggregate to form homomolecular fibrils, monomeric $A\beta_{42}$ strongly catalyzes the aggregation of $A\beta_{40}$.[48] Furthermore, $A\beta_{42}$ has been shown to both co-aggregate with and cross-seed $A\beta$ peptides with N-terminal extensions ranging from 5–40 residues in length.[33] Consequently, it is important to account for the interactions between $A\beta$ alloforms when considering the *in vivo* behavior of these peptides.

Although $A\beta$ alloforms ending before residue 40 are less commonly found in plaques in AD patients and are not directly implicated in the onset of AD, these shorter alloforms are nevertheless important factors to consider in the disease-related aggregation of longer alloforms. Formation of oligomeric co-assemblies might decrease the rate of aggregation by peptides with a higher intrinsic nucleation rate, and acceleration the aggregation of peptides with a lower intrinsic nucleation rate. Indeed, there are indications that these shorter alloforms play an important role *in vivo* by modulating pathogenic $A\beta_{1-42}$ aggregation. It has been shown these shorter alloforms are not inherently toxic, but are in fact neuroprotective in a dose-dependent manner and capable of reducing $A\beta_{1-42}$ deposition.[49,50] It has been proposed that this neuroprotective behavior could be caused by inhibition of $A\beta_{42}$ oligomerization by the shorter alloforms[51,52] or by impeded oligomer conversion to fibrillar structure,[53] as has previously been observed for $A\beta_{40}$.[54,55] The interactions and cross-reactivity between $A\beta$ alloforms other than $A\beta_{1-42}/A\beta_{1-40}$ have, to our knowledge, not been carefully studied.

In this study, we investigate the interactions and cross-reactivity between four $A\beta$ naturally abundant alloforms, $A\beta_{37}$, $A\beta_{38}$, $A\beta_{40}$, and $A\beta_{42}$, with an aim to unravel any cross-catalysis or co-aggregation processes (Fig. 1). Working *in vitro* and using highly purified peptides to maximize reproducibility, we characterize their interactions primarily through kinetic aggregation assays using the fluorescent dye thioflavin T (ThT), the quantum yield of which reports quantitatively on aggregate mass concentration when properly calibrated.[56] We investigate not only the effect that each alloform has on the aggregation of the others in binary mixtures, but also consider three-peptide and four-peptide mixtures in order to better understand how different ratios of $A\beta$ alloforms affects the overall rate of conversion of monomer to amyloid fibril. In these experiments, we ask whether any particular ratio of the shorter length variants will maximally affect the aggregation of $A\beta_{42}$.

Results

The aggregation of $A\beta$(M1-37), $A\beta$(M1-38), $A\beta$(M1-40), and $A\beta$(M1-42) (Fig. 2, referred to herein as $A\beta_{37}$, $A\beta_{38}$, $A\beta_{40}$, and $A\beta_{42}$, respectively) in binary, trinary, and quaternary mixtures was investigated using *in vitro* kinetic assays, analytical high performance liquid chromatography (HPLC), and cryo-transmission electron microscopy (cryo-TEM). First, the

Aβ37: MDAEFRHDSGYEVHHQKLVFFAEDVGSNKGAIIGLMVG

Aβ38: MDAEFRHDSGYEVHHQKLVFFAEDVGSNKGAIIGLMVGG

Aβ40: MDAEFRHDSGYEVHHQKLVFFAEDVGSNKGAIIGLMVGGVV

Aβ42: MDAEFRHDSGYEVHHQKLVFFAEDVGSNKGAIIGLMVGGVVIA

Fig. 2 Amino acid sequences of the peptides investigated in this work.

aggregation of $Aβ_{37}$ or $Aβ_{38}$ in the absence of other peptides was investigated. Next, the aggregation of two-peptide systems, including either $Aβ_{37}$ or $Aβ_{38}$ together with either $Aβ_{40}$ or $Aβ_{42}$, was investigated. Additionally, two-peptide cross-seeding experiments were also performed. Subsequently, three-peptide systems composed of $Aβ_{40}$, $Aβ_{42}$, and either $Aβ_{37}$ or $Aβ_{38}$ were studied. Finally, the aggregation behavior of four-peptide system, including all four alloforms, was investigated. All experiments were performed in 20 mM sodium phosphate buffer, 200 µM ethylenediaminetetraacetic acid (EDTA), 0.02% NaN_3, at pH 7.4, as all alloforms aggregate fast enough to give relatively reproducible data under these conditions. The incorporation of an N-terminal Met residue has no observable effect on the ssNMR spectrum of $Aβ_{42}$ fibrils and aggregation mechanism,[57] and was chosen because it allows for expression "as is" with easy purification without the complication of tags and proteases.[58]

Independent aggregation of $Aβ_{37}$ and $Aβ_{38}$

Before studying the aggregation of $Aβ_{37}$ and $Aβ_{38}$ in hetero-molecular mixtures, the aggregation of each peptide independent of the others was first investigated (Fig. 3). $Aβ_{37}$ and $Aβ_{38}$ displayed greatly reduced aggregation propensity relative to $Aβ_{40}$ and $Aβ_{42}$. In identical conditions and at the low end of the concentration range studied here, $Aβ_{40}$ aggregates within two hours, while $Aβ_{42}$ aggregates within a fraction of an hour.[37,38,41] However, the aggregation propensity among these naturally

occurring Aβ alloforms is evidently not directly correlated to peptide length, as $Aβ_{38}$ was found here to aggregate much more slowly than $Aβ_{37}$.

The aggregation curve shapes for both $Aβ_{37}$ and $Aβ_{38}$ both displayed long lag phases, during which little aggregation was observable above the signal-to-noise ratio, followed by distinct growth phases, in which most aggregate growth happened rapidly. This distinctive curve shape, with a sharp transition between lag and growth phases, is characteristic of an aggregation mechanism driven by a self-replicating, fibril-catalyzed process. The concentration dependence of the rate of aggregation of each peptide was clearly shown by the half-time plots (Fig. 3c), in which the time at which half of the total peptide had aggregated was plotted *versus* starting monomer concentration. The scaling exponent, $γ$, of a power function fitted to the half-time data provides valuable insight into the underlying aggregation mechanism.[59,60] Aggregation mechanisms driven by fragmentation and secondary nucleation, the two self-replicating processes observed in amyloid-related aggregation, display characteristic $γ$ values: for fragmentation-dominated systems, $γ = -0.5$, while for secondary-nucleation-dominated systems $γ \leq -1.0$, with the exact value depending on the reaction order of secondary nucleation and the balance between primary and secondary nucleation, and whether or not secondary nucleation saturates.[38,61] For both $Aβ_{37}$ and $Aβ_{38}$, $γ = -1.0$, indicating that the aggregation of both peptides is driven by secondary nucleation. This is not surprising, as the aggregation of both $Aβ_{40}$ and $Aβ_{42}$ has been shown to be dominated

Fig. 3 The aggregation kinetics of pure solutions of (a) $Aβ_{37}$ and (b) $Aβ_{38}$ in 20 mM sodium phosphate buffer, pH 7.4, with 200 µM EDTA, 0.02% NaN_3, and 20 µM ThT. Three technical replicates are shown for each concentration. (c) Double-logarithmic plot of the aggregation half-time *versus* initial monomer concentration, $[m]_0$, for $Aβ_{37}$ (purple) and $Aβ_{38}$ (blue), where the half-time is the time at which the fluorescence signal is half of its final plateau value. Each dashed line shows a fitted power function with scaling exponent, $γ$. Points show the mean of the three technical replicates, with error bars showing the standard deviation.

by this same process.[37,38] The high variability among technical repeats at low concentrations prevents data fitting to generate a quantitative description of the aggregation process for either peptide, as has previously been done for $A\beta_{40}$ and $A\beta_{42}$.[37,38,62] However, such comprehensive characterization is not required for this study, for which the interactions between different $A\beta$ alloforms, rather than the isolated behavior of any one peptide, is the primary focus.

Aggregation kinetics of mixtures of $A\beta_{40}$ with $A\beta_{37}$ or $A\beta_{38}$

In kinetic assays of the aggregation process in binary mixtures of $A\beta_{40}$ and either $A\beta_{37}$ or $A\beta_{38}$, only a single transition was observed (Fig. 4). This contrasts with the aggregation behavior of monomeric $A\beta_{40}/A\beta_{42}$ mixtures, which produced a double-sigmoidal profile that was found to correspond to the self-assembly of each peptide on distinct timescales into segregated, homomolecular fibrils.[48] The effects of each peptide on the aggregation of the other were studied by holding the concentration of one peptide constant while varying the concentration of the other. The addition of $A\beta_{40}$ to solutions of $A\beta_{37}$ or $A\beta_{38}$ decreased the lag time before the single observed fluorescence transition (Fig. 4a and b). Conversely, with a constant concentration of $A\beta_{40}$, the addition of either $A\beta_{37}$ or $A\beta_{38}$ resulted in a delay in aggregation (Fig. 4c and d). In both

cases, the addition of the shorter alloform to $A\beta_{40}$ results in an increase in the intensity of ThT fluorescence, indicating that the shorter alloforms are aggregating concurrently with $A\beta_{40}$, rather than at a later timepoint. The modulation of the kinetics of aggregation for both peptides in both $A\beta_{37}/A\beta_{40}$ and $A\beta_{38}/A\beta_{40}$ mixtures, as well as the fact that a monophasic aggregation profile is observed at all molar ratios tested despite the differing timescales of the independent aggregation of $A\beta_{37}$ and $A\beta_{38}$ compared to that of $A\beta_{40}$, suggest that these peptides may co-aggregate to form some level of mixed aggregates. However, ThT fluorescence assays, which report only on total aggregate mass concentration, cannot distinguish co-aggregates from coexisting homomolecular fibrils.

The ultrastructure of the aggregates formed by these peptides, both alone and in mixtures, was investigated using cryo-TEM (Fig. 5). Images were collected of fibrils produced by each peptide individually, as well as by those formed by equimolar $A\beta_{37}/A\beta_{40}$ and $A\beta_{38}/A\beta_{40}$ mixtures. Samples were prepared in the same manner as for the kinetic assays, with fibril formation monitored by ThT fluorescence. The samples were frozen on grids once the final fluorescence plateau was reached. All of the fibrils formed from a pure peptide solution display relatively consistent morphology. Moreover, these homomolecular fibrils were morphologically similar between peptides: the fibrils formed by $A\beta_{37}$, $A\beta_{38}$, and $A\beta_{40}$ had average

Fig. 4 Aggregation kinetics of two-peptide systems composed of $A\beta_{40}$ with (a & c) $A\beta_{37}$ and (c & d) $A\beta_{38}$ in 20 mM sodium phosphate buffer, pH 7.4, with 200 μM EDTA, 0.02% NaN₃, and 20 μM ThT. The effect of $A\beta_{40}$ at varying concentrations on the aggregation of (a) $A\beta_{37}$ or (b) $A\beta_{38}$. Aggregation kinetics for $A\beta_{40}$ alone at the same concentrations are shown in Fig. S1.† The effect of varying concentrations of (c) $A\beta_{37}$ or (d) $A\beta_{38}$ on the aggregation of $A\beta_{40}$. The extended time-courses for (c) and (d) are shown in Fig. S2.†

Fig. 5 The morphology of fibrils formed by $A\beta_{37}$, $A\beta_{38}$, and $A\beta_{40}$ in pure and equimolar binary solutions. (a) Representative cryo-TEM images of fibrils. Fibrils were formed in 20 mM sodium phosphate buffer, pH 7.4, with 200 μM EDTA, 0.02% NaN_3, and 20 μM ThT. (b) Quantification of fibril node-to-node distance (half-pitch period). Representative grey scale profiles used for helical half-pitch period measurements are shown in Fig. S3.† (c) Quantification of fibril diameter. Plots represent >50 measurements, taken from at least 15 different fibrils. **$p \leq 0.01$, ***$p \leq 0.001$, and ****$p \leq 0.0001$ by one-way ANOVA followed by Dunnett's post-hoc test.

helical half-pitch periods of 118 ± 30 nm, 131 ± 40 nm, and 125 ± 22 nm and average fibril diameters of 19 ± 6 nm, 15 ± 5 nm, and 18 ± 4, respectively. Notably, the morphology of the fibrils formed by each of these peptides was significantly different than that of the fibrils formed by $A\beta_{42}$, which have a helical half pitch of 31 ± 17 nm.[48] The fibrils formed from binary mixtures, on the other hand, displayed distinct morphology. For both $A\beta_{37}/A\beta_{40}$ and $A\beta_{38}/A\beta_{40}$ mixtures, fibrils were observed with helical half-pitch periodicities that did not correspond to the fibrils formed independently by either of the peptides present in the reaction mixture. In both cases, the average fibril half-pitch period (160 ± 90 nm for $A\beta_{37}/A\beta_{40}$ and 183 ± 106 for $A\beta_{38}/A\beta_{40}$) was both significantly longer and more variable than for any of the homomolecular fibrils (Fig. 5b). Additionally, the average width of the fibrils formed in each binary mixture (21 ± 10 nm for $A\beta_{37}/A\beta_{40}$ and 23 ± 12 for $A\beta_{38}/A\beta_{40}$) was both larger and more variable than for either of the constituent peptides, although this was statistically significant only for $A\beta_{38}/A\beta_{40}$ (Fig. 5c). The presence in both binary systems of fibrils with morphology distinct from those of homomolecular fibrils formed by either constituent peptide provided further evidence that some level of co-aggregation had occurred both between $A\beta_{37}$ and $A\beta_{40}$ and between $A\beta_{38}$ and $A\beta_{40}$.

Aggregation kinetics of mixtures of $A\beta_{42}$ with $A\beta_{37}$ or $A\beta_{38}$

Following the investigation of the aggregation behavior of $A\beta_{40}$ with $A\beta_{37}$ and $A\beta_{38}$, similar experiments were performed on two-

peptide systems with $A\beta_{42}$ (Fig. 6). Starting from monomeric $A\beta_{37}/A\beta_{42}$ or $A\beta_{38}/A\beta_{42}$ mixtures, two distinct transitions were observed in the curves as monitored by ThT fluorescence. Such biphasic aggregation profiles were previously observed for the aggregation of a mixture of $A\beta_{40}$ and $A\beta_{42}$, which was found to correspond to aggregation into separate fibrils.[48] This indicates that the nature of the interactions of these shorter alloforms with $A\beta_{42}$ are quite different than with $A\beta_{40}$. The biphasic profile suggests that two separate aggregation processes are occurring on discrete timescales, consistent with the formation of homomolecular fibrils.

There were nevertheless significant interactions between the two peptides present in both $A\beta_{37}/A\beta_{42}$ and $A\beta_{38}/A\beta_{42}$ mixtures, as evidenced by the changes to the timescale of aggregation of both peptides in the mixture. The presence of $A\beta_{42}$ strongly accelerated the aggregation of both $A\beta_{37}$ and $A\beta_{38}$ (Fig. 6a and b, respectively) by dramatically shortening their lag phases. Notably, each of $A\beta_{37}$ and $A\beta_{38}$ clearly inhibited the aggregation of $A\beta_{42}$ (Fig. 6c and d, respectively), although this effect is less dramatic than the reciprocal acceleration of both $A\beta_{37}$ and $A\beta_{38}$ aggregation by $A\beta_{42}$.

The aggregation of $A\beta_{42}$ is known to proceed through three distinct processes: primary (non-fibril-catalyzed) nucleation, secondary (fibril-catalyzed) nucleation, and elongation.[37] To inhibit aggregation, an effector must perturb one or more of these processes. Inhibition of each of the processes affects the kinetics of aggregation in a distinct manner,[14,63] meaning that

Fig. 6 Aggregation kinetics of two-peptide systems composed of $A\beta_{42}$ with (a & c) $A\beta_{37}$ and (b & d) $A\beta_{38}$ in 20 mM sodium phosphate buffer, pH 7.4, with 200 μM EDTA, 0.02% NaN_3, and 20 μM ThT. (a and b) Increasing $A\beta_{42}$ concentration leads to accelerated aggregation of $A\beta_{37}$ and $A\beta_{38}$, respectively. Aggregation kinetics for $A\beta_{42}$ alone at the same concentrations are shown in Fig. S1.† (c and d) Increasing concentrations of $A\beta_{37}$ and $A\beta_{38}$, respectively, decrease the rate of $A\beta_{42}$ aggregation; in both, the upper panel shows the first, low-intensity fluorescence transition and the lower panel shows the full biphasic aggregation profile.

the change in the $A\beta_{42}$ curve shape in the presence of each of the shorter alloforms can, in principle, be used to determine which process is being inhibited. Using the AmyloFit program,[59] a model of secondary-nucleation-dominated aggregation was fit to the data shown in Fig. 6c and d; the parameters corresponding to the rate of each process were, one-by-one, allowed to vary while all other parameters were held constant (Fig. 7). This analysis shows that the observed changes to the curve shape of $A\beta_{42}$ aggregation in the presence of both $A\beta_{37}$ and $A\beta_{38}$ is poorly modeled by inhibition of primary nucleation (Fig. 7a and d, respectively). However, the change to the $A\beta_{42}$ aggregation curve shape, although significant, is too small for the kinetic analysis to distinguish between inhibition of secondary nucleation (Fig. 7b and e) and inhibition of elongation (Fig. 7c and f). Nevertheless, this fitting indicates that the inhibition of

$A\beta_{42}$ aggregation by both $A\beta_{37}$ and $A\beta_{38}$ involves interaction between the shorter peptide and the $A\beta_{42}$ fibril, as both secondary nucleation and elongation are fibril-catalyzed processes.

Cross-seeding of $A\beta_{37}$ and $A\beta_{38}$ with $A\beta_{40}$ and $A\beta_{42}$

Having studied the aggregation in systems composed of two Aβ alloforms, both starting in a monomeric state, we next investigated whether any of these peptide mixtures displayed cross-seeding behavior. In aggregating systems driven by a fibril-catalyzed secondary nucleation process, as is the case for all Aβ alloforms studied here, the addition of pre-aggregated seed fibrils to a solution of monomer can accelerate aggregation by providing a catalytic surface for nucleation from the start of the reaction process. The self-seeding of both $A\beta_{42}$ and $A\beta_{40}$ is well

Fig. 7 Fitting different models of inhibition to aggregation kinetics of 3 μM Aβ$_{42}$ with varying concentrations of (a–c) Aβ$_{37}$ and (d–f) Aβ$_{38}$; the data are the same as are shown in Fig. 6c and d, respectively. The models used here correspond to inhibition of (a & d) primary nucleation, (b & e) secondary nucleation, and (c & f) elongation processes. (g) Mean residual errors for fitting shown in (a–f), normalized to the error for the best fit for each data set. Errors for Aβ$_{37}$/Aβ$_{42}$ fitting are shown in purple and errors for Aβ$_{38}$/Aβ$_{42}$ fitting are shown in blue.

established.[37,38,64] Although Aβ$_{40}$ and Aβ$_{42}$ have been shown to display some cross-seeding behavior, these effects are only evident at high seed concentrations (0.5 and 1 μM Aβ$_{40}$ seed added to 2 μM Aβ$_{42}$ monomer) and are much weaker than those observed for self-seeding.[48]

In cross-seeding reactions, interactions between the monomeric peptide and the surface of the seed fibril can result in divergent kinetic outcomes.[65] The seed fibril can serve as a surface for heterogenous primary nucleation, wherein monomer adsorption by the fibril increases local monomer concentration, thereby catalyzing aggregation.[66,67] Conversely, higher-affinity monomer adsorption by the fibril surface leads to monomer sequestration, thus reducing the overall rate of aggregation, particularly during the fibril growth phase.[48,67] In previous cross-seeding reactions between Aβ$_{40}$ and Aβ$_{42}$, Aβ$_{42}$ seeds were shown to have no effect on Aβ$_{40}$ aggregation; although high concentrations of Aβ$_{40}$ seeds (25–50%) were shown to affect Aβ$_{42}$ aggregation, these effects were much weaker than those of the self-seeding of Aβ$_{42}$.[48]

Here, we found that the aggregation of Aβ$_{37}$ is catalyzed by the presence of seeds of any of the four peptides (Fig. 8a). The effects were most dramatic for the self-seeding of Aβ$_{37}$ (purple) and Aβ$_{38}$ (blue), although they were nevertheless significant in all three cross-seeding cases. For the cross-seeding of Aβ$_{37}$ with Aβ$_{40}$ fibrils (green), the addition of seeds not only decreased the duration of the lag phase, but also reduced the slope of the curve during the aggregate growth phase. In contrast, either Aβ$_{38}$ (blue) or Aβ$_{42}$ (red) seed shortened the lag phase with minimal effects on the curve shape. This reduction in lag phase without a concomitant change in the curve shape suggests that

the likely cause of the acceleration is the provision of a catalytic surface for the heterogeneous primary nucleation of Aβ$_{37}$. However, at such long lag times, variability between experimental repeats is inevitable and prevents explicit verification of this proposed mechanism through fitting to kinetic models. Notably, the catalytic effect of Aβ$_{42}$ fibrils on Aβ$_{37}$ aggregation was smaller than that of monomeric Aβ$_{42}$ at comparable concentrations (Fig. 6a), indicating that monomer–monomer interactions are a significant factor in the catalysis of Aβ$_{37}$ aggregation by Aβ$_{42}$. The fact that some cross-seeding behavior was observed, however, indicates that interactions between monomeric Aβ$_{37}$ and fibrillar Aβ$_{42}$ do also occur. This is consistent with the conclusions drawn from mechanistic fitting to the data of Aβ$_{42}$ aggregation in the presence of monomeric Aβ$_{37}$ (Fig. 7a–c).

As with Aβ$_{37}$, the acceleration of Aβ$_{38}$ aggregation was stronger in the self-seeded case than for cross-seeding (Fig. 8b). At high concentrations of Aβ$_{38}$ seed, there was essentially no lag phase, with significant quantities of fibrils formed almost instantaneously. Having already found that Aβ$_{38}$ fibrils can seed the aggregation of monomeric Aβ$_{37}$ (Fig. 8a), the reciprocal effect is also observed, with the addition of Aβ$_{37}$ seeds accelerating Aβ$_{38}$ aggregation. For the cross-seeding of Aβ$_{38}$ with both Aβ$_{40}$ and Aβ$_{42}$ seed fibrils, a clear concentration-dependent decrease in the lag time was observed; in both cases, there was no perturbation to the aggregation curve shape.

For Aβ$_{40}$, clear self-seeding behavior was observed (Fig. 8c), consistent with previous findings.[38,48] Additionally, clear reduction in the duration of the lag time was observed with the addition of both Aβ$_{37}$ and Aβ$_{38}$ seed fibrils, particularly at

Fig. 8 Self- and cross-seeding experiments for monomeric (a) $A\beta_{37}$, (b) $A\beta_{38}$, (c) $A\beta_{40}$, and (d) $A\beta_{42}$. In all panels, the color of the frame corresponds to the identity of the monomeric peptide and the color of the kinetic curves corresponds to the identity of the seed peptide, with $A\beta_{37}$, $A\beta_{38}$, $A\beta_{40}$, and $A\beta_{42}$ represented by purple, blue, green, and red, respectively. Seed concentrations are given as a molar percentage of the monomer concentration. The rightmost panel in each row shows the aggregation half-time as a function on seed percentage. $A\beta_{37}$, $A\beta_{38}$, and $A\beta_{40}$ monomer solutions were prepared to a peptide concentration of 10 μM, and $A\beta_{42}$ was prepared to a monomer concentration of 3 μM. All experiments were performed in 20 mM sodium phosphate buffer, pH 7.4, with 200 μM EDTA, 0.02% NaN₃, and 20 μM ThT.

relatively high seed concentrations. As is the case for both $A\beta_{37}$ and $A\beta_{38}$, however, this cross-seeding effect was again weaker than the self-seeding effect. Similar to what was observed for the seeding of $A\beta_{37}$ monomer with $A\beta_{40}$ fibrils, the addition of $A\beta_{37}$ fibrils to $A\beta_{40}$ monomer affected not only the lag phase but also the slope of the curve during the aggregate growth phase. Indeed, at low concentrations of $A\beta_{37}$ seed fibrils, this inhibitory effect was more significant than the reduction of the lag phase, resulting in an increase of the aggregation half-time relative to unseeded $A\beta_{40}$.

Clear self-seeding behavior was observed for $A\beta_{42}$, as has been reported previously;[37,48] however, no cross-seeding catalysis was observed with either $A\beta_{37}$ or $A\beta_{38}$ seed fibrils (Fig. 8d). Even at high concentrations of $A\beta_{37}$ and $A\beta_{38}$ seed fibrils, both the timescale and curve shape of $A\beta_{42}$ aggregation were completely unperturbed, indicating that these foreign aggregates are inert with respect to monomeric $A\beta_{42}$, neither providing a surface for heterogeneous nucleation nor sequestering monomer. This suggests that the inhibition of $A\beta_{42}$ aggregation observed in the presence of $A\beta_{37}$ or $A\beta_{38}$ (Fig. 6c and

d, respectively) was caused by monomeric or oligomeric, rather than fibrillar, species. This is especially relevant given that, at the point in time at which $A\beta_{42}$ aggregates, both $A\beta_{37}$ and $A\beta_{38}$ will be in a primarily monomeric state, due to the relatively slow aggregation of both peptides.

Aggregation kinetics of three-peptide mixtures

Having characterized the effects that the presence of either monomeric or fibrillar species of each $A\beta$ alloform had on aggregation kinetics of the others, we next studied the behavior of $A\beta_{37}$ or $A\beta_{38}$ in three-peptide monomeric mixtures with $A\beta_{40}$ and $A\beta_{42}$. For both the $A\beta_{37}/A\beta_{40}/A\beta_{42}$ and the $A\beta_{38}/A\beta_{40}/A\beta_{42}$ mixtures, two discrete transitions in ThT fluorescence were observed, separated by an intermediate plateau phase (Fig. 9a and c, respectively). This is consistent with two aggregation processes happening on distinct timescales. The intensity of the second transition in ThT fluorescence increased with increasing

concentration of $A\beta_{37}$ or $A\beta_{38}$, indicating that both peptides aggregate as part of the second, slower process. Based on the previous monomeric two-peptide aggregation kinetic assays (Fig. 4 and 6), it is most likely that the first fluorescence transition here represents the aggregation of $A\beta_{42}$, with the second transition showing the co-aggregation of $A\beta_{40}$ and $A\beta_{37}$ or $A\beta_{38}$.

To analyze the identity and composition of the peptide aggregates that have formed during each transition, analytical HPLC was used to determine the concentration of each peptide over the time-course of the aggregation of an equimolar three-peptide mixture (Fig. 10). To characterize the composition of fibrillar species, aliquots were removed during the initial lag phase (t_L) and each plateau phase (t_{P1} and t_{P2}) (Fig. 10b and c for mixtures including $A\beta_{37}$ and $A\beta_{38}$, respectively). The fibrils present in these aliquots were isolated by centrifugation, washed to remove any oligomers associated with the fibril surface, then dissolved and injected on an HPLC instrument. In
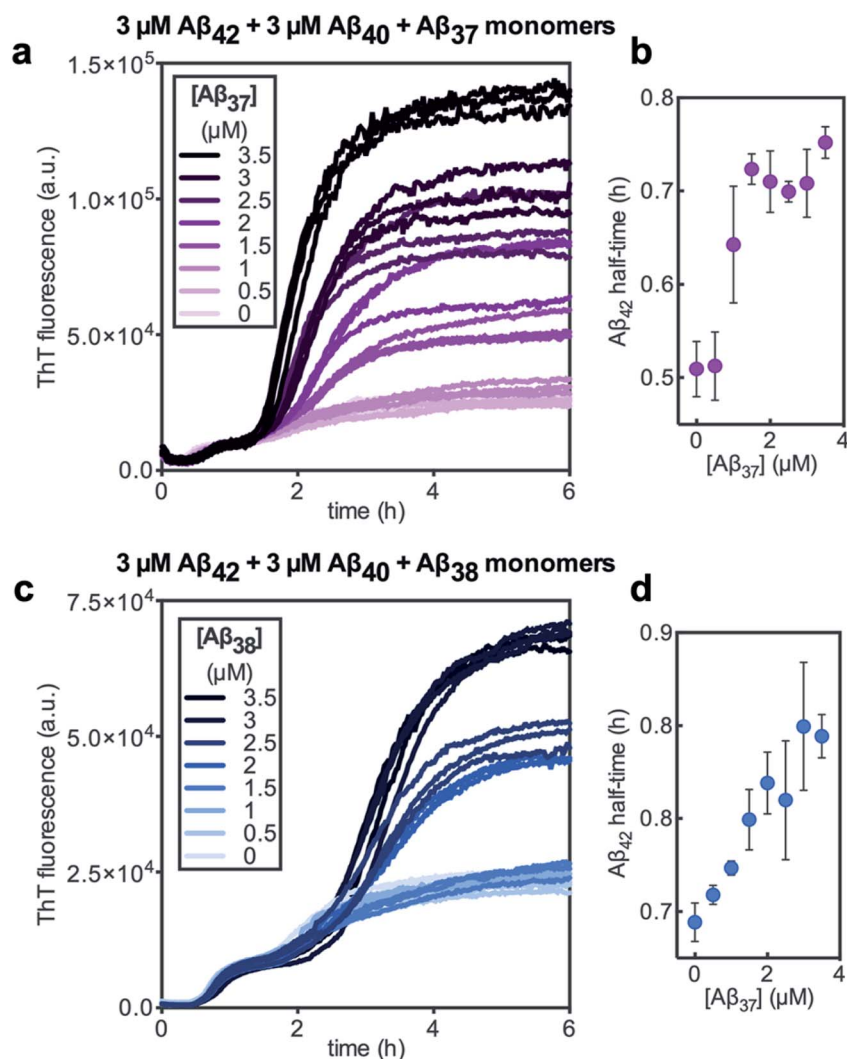

Fig. 9 Aggregation of three-peptide systems composed of 3 μM each $A\beta_{40}$ and $A\beta_{42}$, with varying concentrations of (a and b) $A\beta_{37}$ or (c and d) $A\beta_{38}$ in 20 mM sodium phosphate buffer, pH 7.4, with 200 μM EDTA, 0.02% NaN₃, and 20 μM ThT. Panels (a) and (c) show the aggregation kinetics curves. Panels (b) and (d) show the half-time of $A\beta_{42}$ aggregation plotted as a function of $A\beta_{37}$ and $A\beta_{38}$ concentration, respectively. The points represent the average of the three technical triplicates, with the error bars showing the standard deviation.

Fig. 10 Alloform composition in fibrillar and monomeric species over the time-course of aggregation of trimolecular mixtures of 3 μM each $A\beta_{40}$, $A\beta_{42}$, and either (b & d) $A\beta_{37}$ or (c & e) $A\beta_{38}$, as analyzed using analytical HPLC. (a) A representative kinetic aggregation curve, with the time points at which aliquots were removed marked with red lines. (b & c) The composition of fibrillar species during the lag phase and each plateau phase. (d & e) The composition of monomeric species during the lag phase, both transition phases, and both plateau phases. Kinetic experiments were performed in 20 mM sodium phosphate, 200 μM EDTA, 0.02% NaN_3, pH 7.4, with 20 μM ThT.

both three-peptide mixtures, it was found that the fibrils present in the intermediate plateau phase were primarily composed of $A\beta_{42}$, while the fibrils in the final plateau phase were composed of all three peptides. These data are supported by the complementary analysis of the peptide composition of the supernatants (Fig. 10d and e), for which additional aliquots were taken during each aggregate growth phase (t_{G1} and t_{G2}). For both $A\beta_{37}/A\beta_{40}/A\beta_{42}$ and $A\beta_{38}/A\beta_{40}/A\beta_{42}$ mixtures, it was found that the concentration of monomeric $A\beta_{42}$ decreased during the first transition in ThT fluorescence and was undetectable by the intermediate plateau phase. During the second transition phase, the concentration of both $A\beta_{40}$ and either $A\beta_{37}$ or $A\beta_{38}$ decreased. At the final plateau phase, the majority of peptides were converted to fibrils and the monomer concentration was below the detection limit of analytical HPLC. This indicates that, in these three-peptide mixtures, the behavior of

each peptide is consistent with the behavior to in two-peptide systems, with $A\beta_{42}$ forming fibrils during the first transition and $A\beta_{40}$ co-aggregating with $A\beta_{37}$ or $A\beta_{38}$ during the second transition.

Despite aggregating separately from $A\beta_{42}$, the presence of either $A\beta_{37}$ or $A\beta_{38}$ perturbed the kinetics of $A\beta_{42}$ aggregation, as was previously observed in two-peptide systems (Fig. 6c and d). The half-time of $A\beta_{42}$ aggregation increased with increasing concentration of either $A\beta_{37}$ or $A\beta_{38}$ (Fig. 9b and d, respectively), with the half-time of $A\beta_{42}$ aggregation defined here as the time at which the fluorescence intensity reached half-way between the initial baseline and the intermediate plateau. This shows that $A\beta_{37}/A\beta_{42}$, $A\beta_{38}/A\beta_{42}$, and $A\beta_{40}/A\beta_{42}$ (ref. 48) interactions observed in two-peptide systems persist in three-peptide systems.

Fig. 11 (a) The aggregation of 3 μM Aβ$_{42}$ with varying concentrations of a 1 : 1 : 1 mixture of Aβ$_{37}$/Aβ$_{38}$/Aβ$_{40}$. (b) The half-time of the aggregation of Aβ$_{42}$ shown in (a) *versus* the total concentration of the three shorter alloforms. Kinetic experiment was performed in 20 mM sodium phosphate buffer, pH 7.4, with 200 μM EDTA, 0.02% NaN$_3$, and 20 μM ThT.

Aggregation kinetics of four-peptide mixtures

Finally, the aggregation behavior in monomeric mixtures of all four alloforms was studied. First, the aggregation of 3 μM Aβ$_{42}$ in mixtures with varying concentrations of Aβ$_{37}$, Aβ$_{38}$, and Aβ$_{40}$ at an equimolar ratio was characterized (Fig. 11). For all four-peptide mixtures, two distinct transitions in ThT fluorescence intensity were observed. The intensity of the second transition (which was absent in a solution containing only Aβ$_{42}$) scaled with increasing concentration of the Aβ$_{37}$/Aβ$_{38}$/Aβ$_{40}$ mixture, while the intensity of the first transition did not. This indicates that all three of the shorter Aβ alloforms may form co-aggregates, while Aβ$_{42}$ aggregates first, forming separate fibrils. As would be expected given the behavior observed in three-peptide mixtures, the aggregation of Aβ$_{42}$ was perturbed by the presence of shorter Aβ alloforms despite the slower aggregation of these peptides, with increasing concentrations of the short-alloform mixture leading to longer Aβ$_{42}$ aggregation half-times (Fig. 11b).

We next characterized the relative effects of each of the shorter Aβ alloforms on the aggregation of Aβ$_{42}$, with an aim to determine whether specific ratios of these alloforms would maximally affect Aβ$_{42}$ aggregation. For this, the aggregation of 3 μM Aβ$_{42}$ was studied in the presence of a constant total concentration (6 μM) of mixtures of Aβ$_{37}$, Aβ$_{38}$, and Aβ$_{40}$, with these three peptides in varying ratios (Fig. 12). For each ratio tested, only two fluorescence transitions were observed, providing further evidence that the three shortest alloforms co-aggregate irrespective of their ratio. Both the timescale and intensity of the second transition varied based on the ratio of Aβ$_{37}$, Aβ$_{38}$, and Aβ$_{40}$, due to the differing aggregation propensities and ThT quantum yielded of each peptide. The aggregation of Aβ$_{42}$ was found to be inhibited by all solutions tested, irrespective of the peptide ratios, although to varying extents. Included in this study were 6 μM each Aβ$_{37}$, Aβ$_{38}$, and Aβ$_{40}$ alone, to allow for side-by-side comparison of the degree to which each alloform inhibits Aβ$_{42}$ aggregation. Of the three, Aβ$_{38}$ inhibited the aggregation of Aβ$_{42}$ to the greatest degree, followed by Aβ$_{37}$ and Aβ$_{40}$. This was found to be reproducible between repeats of the whole experiment. Notably, mixtures of all three peptides produced a stronger inhibitory effect than any single peptide alone. Although the relative strength of inhibition of these different mixtures was not found to be highly reproducible between repeats of the experiment, mixtures with higher concentrations of Aβ$_{38}$ generally exhibited stronger inhibitory effects than did mixtures with low concentrations of Aβ$_{38}$. Still, Aβ$_{38}$ alone was not the most effective, with the strongest inhibition observed at the 2 : 3 : 1 and 1 : 4 : 1 ratios of Aβ$_{37}$: Aβ$_{38}$: Aβ$_{40}$.

Discussion

The results of this study points to significant cross-reactivity in quaternary mixtures of Aβ$_{42}$ and shorter alloforms, beyond those observed in binary mixtures.[48] Notably, both monomeric Aβ$_{37}$ and Aβ$_{38}$ appear to interact with Aβ$_{42}$ in much the same manner as does monomeric Aβ$_{40}$. Most fundamentally, all three of the shortest alloforms aggregate independently of Aβ$_{42}$, giving rise to two distinct fluorescence transitions. Furthermore, similar reciprocal kinetic effects are observed in binary

Fig. 12 Aggregation kinetics of 3 μM Aβ$_{42}$ with 6 μM of Aβ$_{37}$/Aβ$_{38}$/Aβ$_{40}$ mixtures in varying molar ratios. (a) The first ThT transition, corresponding to the aggregation of Aβ$_{42}$ is shown; the full aggregation profiles are shown in Fig. S4.† (b) The half-times of Aβ$_{42}$ aggregation in (a), *versus* the concentration of Aβ$_{37}$ (green panel), Aβ$_{38}$ (blue panel), and Aβ$_{40}$ (red panel). The color of each point corresponds to the curves of the same color in (a). (c) Triangular heat-map representation of the half-time of Aβ$_{42}$ aggregation depending on the Aβ$_{37}$/Aβ$_{38}$/Aβ$_{40}$ concentrations. Experiments were performed in 20 mM sodium phosphate buffer, pH 7.4, with 200 μM EDTA, 0.02% NaN$_3$, and 20 μM ThT.

monomeric mixtures of $A\beta_{42}$ with each of the three shorter alloforms. As was found here for both $A\beta_{37}$ and $A\beta_{38}$, the presence of monomeric $A\beta_{42}$ accelerates the aggregation of $A\beta_{40}$ by significantly shortening the lag phase,[48] although this effect is significantly more pronounced with $A\beta_{37}$ and $A\beta_{38}$, which both aggregate much more slowly than $A\beta_{40}$. Additionally, the presence of any of the three shortest alloforms serves to inhibit the aggregation of $A\beta_{42}$. In each case, this effect is weaker than the reciprocal $A\beta_{42}$-induced acceleration of aggregation of the shorter alloform.

The cross-seeding between $A\beta_{42}$ and each of the shorter alloforms showed a stronger dependence on alloform length. As reported by Cukalevski *et al.*, the addition of $A\beta_{42}$ seeds to $A\beta_{40}$ monomers results in minimal change to the kinetics of $A\beta_{40}$ aggregation.[48] This contrasts with the cross-seeding interactions between $A\beta_{42}$ seeds and both $A\beta_{37}$ and $A\beta_{38}$ monomers, for which a clear $A\beta_{42}$-concentration-dependent decrease in the aggregation half-time of the shorter alloform was observed in both cases. Furthermore, Cukalevski *et al.* reported that the addition of high concentrations of $A\beta_{40}$ seeds to $A\beta_{42}$ monomers leads to a moderate reduction of both the lag time and the rate of $A\beta_{42}$ aggregation during the fibril growth phase (these converse effects largely cancel out, leaving the half-time of $A\beta_{42}$ essentially unchanged).[48] This behavior differs from the interactions observed here for the cross-seeding of $A\beta_{42}$ monomers with either $A\beta_{37}$ or $A\beta_{38}$, for which even high seed concentrations had no effect on the kinetics of $A\beta_{42}$ aggregation.

The results of this study serve to extend our understanding of interactions between $A\beta$ alloforms by investigating the aggregation behavior of tri- and tetra-molecular mixtures. The fact that $A\beta_{37}$, $A\beta_{38}$, and $A\beta_{40}$ each affected $A\beta_{42}$ aggregation to a different extent indicates that inhibition of $A\beta_{42}$ aggregation by these shorter alloforms is not simply due to non-specific interactions with $A\beta_{42}$, but rather includes some level of sequence specificity. That $A\beta_{38}$ is a more potent inhibitor of $A\beta_{42}$ aggregation than are either $A\beta_{37}$ or $A\beta_{40}$ indicates that this effect is not directly correlated to alloform length. Likewise, this inhibition does not appear to be correlated with aggregation propensity, as $A\beta_{37}$ and $A\beta_{40}$ inhibited $A\beta_{42}$ aggregation to a similar extent, despite $A\beta_{40}$ displaying a much higher intrinsic aggregation rate than $A\beta_{37}$. Determination of the various factors, including peptide length and sequence, that affect the relative inhibitory potency of these shorter alloforms towards $A\beta_{42}$ aggregation would provide greater physical insight into the interactions that underlie this inhibition.

Notably, the results of this study indicate that, in addition to being alloform-specific, the effect of short $A\beta$ alloforms on the aggregation of $A\beta_{42}$ is inherently cooperative. Were this inhibition non-cooperative, it would be expected that the decrease in $A\beta_{42}$ aggregation would simply scale with the relative concentrations of the short alloforms. Instead, a mixture of these shorter alloforms affected the rate of $A\beta_{42}$ aggregation more significantly than any single alloform independently, with the strongest inhibition seen at the 2 : 3 : 1 and 1 : 4 : 1 $A\beta_{37}$- : $A\beta_{38}$: $A\beta_{40}$ ratios. While the underlying molecular interactions that give rise to this cooperative inhibition are not readily evident, these results further buttress the conclusion that

inhibition of $A\beta_{42}$ aggregation by shorter $A\beta$ alloforms is sequence specific. One possible explanation for inhibition observed in certain quaternary mixtures may be the formation of mixed oligomers that cannot readily convert to fibrils and that compete for catalytic sites on the fibril surface with more conversion-competent homomolecular oligomers.[68] Although $A\beta_{42}$ in heteromolecular mixtures aggregates at reduced rate compared to pure $A\beta_{42}$, it seems to promote nucleation of $A\beta_{37}$, $A\beta_{38}$ and $A\beta_{40}$ in these mixed oligomers, and after $A\beta_{42}$ has formed homomolecular fibrils, these three peptides seem form joint fibrils with different morphology than any of the pure fibrils of $A\beta_{37}$, $A\beta_{38}$ and $A\beta_{40}$.

When studied alone as single peptides at a range of concentrations, $A\beta_{38}$ appears to aggregate much more slowly than $A\beta_{37}$. The origin of this difference is not clear but may be a consequence of primary or secondary nucleation being less effective with the extra Gly residue at the C-terminus of $A\beta_{38}$. In general, longer sequences aggregate more slowly if the additional length difference lies in a non-amyloidogenic segment.[33,69,70]

These results suggest that in the brain extracellular fluids, where a number of different short $A\beta$ alloforms are present, the disease-associated aggregation of $A\beta_{1-42}$ may in fact be modulated by these short alloforms and, furthermore, that the rate of $A\beta_{1-42}$ aggregation may be sensitive to specific ratios of these alloforms. The relevance of these findings is further underscored by the disease-promoting effect of familial AD-causing presenilin mutations, which lead to a loss of $A\beta_{1-37}$ and $A\beta_{1-38}$ whilst affecting neither $A\beta_{1-40}$ nor $A\beta_{1-42}$ production.[71]

Conclusions

In this study, we show that the $A\beta$ alloforms $A\beta_{37}$ and $A\beta_{38}$ both aggregate through a secondary nucleation driven process to form β-sheet rich fibrils. The aggregation of both of these peptides is comparable to the well-characterized aggregation processes of $A\beta_{40}$ and $A\beta_{42}$, although the aggregation of the shorter two alloforms is significantly slower, which is consistent with their reduced aggregation propensity *in vivo*. Furthermore, we find that the aggregation of all four $A\beta$ alloforms is highly sensitive to the presence of other alloforms. Both $A\beta_{37}$ and $A\beta_{38}$ co-aggregate with $A\beta_{40}$, forming fibrils that are ultrastructurally distinct from the fibrils formed by either of the constituent peptides alone. Furthermore, the kinetics of aggregation in these binary mixtures is highly dependent on the ratio of $A\beta_{37}$/ $A\beta_{40}$ or $A\beta_{38}$/$A\beta_{40}$ present in solution. In contrast to their co-aggregation with $A\beta_{40}$, we find that both $A\beta_{37}$ and $A\beta_{38}$ aggregate independently from $A\beta_{42}$. There is nevertheless significant kinetic modulation between $A\beta_{42}$ and both $A\beta_{37}$ and $A\beta_{38}$, with the shorter alloforms impeding the aggregation of $A\beta_{42}$ in a concentration-dependent manner and $A\beta_{42}$ reciprocally accelerating the aggregation of the shorter alloforms. Finally, we find that the aggregation of $A\beta_{42}$ is sensitive to the specific ratio of shorter alloforms present, indicating a level of sequence specificity in these interactions; we furthermore demonstrate that a mixture of $A\beta_{37}$, $A\beta_{38}$, and $A\beta_{40}$ more potently affects $A\beta_{42}$

aggregation than any one of the shorter alloforms alone, indicating that this inhibition is inherently cooperative.

These results demonstrate that interactions between Aβ alloforms significantly modulate the aggregation behavior of these peptides *in vitro*. As the presence of $A\beta_{38}$ has been shown to attenuate $A\beta_{42}$ fibril formation and deposition *in vivo*,[49,50] it is likely that the interactions described here are pertinent to the biological behavior of these peptides. Indeed, short Aβ alloforms, which make up as much as 90% of the Aβ peptide present in the extracellular fluid of the brain, may play a pathologically relevant role in moderating the aggregation of $A\beta_{42}$. These results are relevant not only to understanding the pathogenesis of AD, but also to the development of AD therapeutics. As modulation of γ-secretase activity is increasingly being proposed as a promising route to AD therapeutics,[72–74] an understanding of how different Aβ alloforms—and how different combinations of these alloforms—affect pathological $A\beta_{42}$ aggregation is becoming increasingly important.

Materials and methods

Expression and purification of Aβ peptides

The genes encoding wild-type Aβ(M1-42), Aβ(M1-40), Aβ(M1-38), and Aβ(M1-37) (referred to herein as $A\beta_{42}$, $A\beta_{40}$, $A\beta_{38}$, and $A\beta_{37}$, respectively) were produced by overlapping PCR and cloned into the PetSac vector.[58] The peptides were expressed in *E. coli* strains BL21 Star (DE3) pLysS (for $A\beta_{42}$, $A\beta_{40}$, and $A\beta_{37}$) or BL21-Gold (DE3) pLysS (for $A\beta_{38}$). Cells were cultured in LB medium with 50 mg L^{-1} ampicillin and (for BL21 Star cells) 30 mg L^{-1} chloramphenicol. Well-isolated bacterial colonies were used to inoculate 50 mL cultures grown in 250 mL baffled flasks at 37 °C with 130 rpm shaking for *ca.* 7 h. Once an OD of 0.7–1.0 was reached, 500 μL of these cultures were then added to 500 mL LB medium (containing the relevant antibiotics, as detailed above) in 2 L baffled flasks, which were grown at 37 °C with 125 rpm shaking for *ca.* 15 h. Cells were then harvested by centrifugation at 6000 × *g* for 10 min at 4 °C.

The peptides were isolated from inclusion bodies after iterative sonication and centrifugation. The inclusion bodies were dissolved in 8 M urea in 10 mM Tris–HCL, pH 8.5, 1 mM EDTA, and the peptide purified by ion exchange chromatography on a DEAE cellulose resin, as previously described.[58] The purity of the eluted fractions was assessed by SDS-PAGE. The purest fractions were pooled. Monomer isolation and removal of inclusion-body-bound proteins was achieved by filtration using 30 kDa MWCO filters, and size exclusion chromatography on a 26 × 600 mm Superdex 75 column. The peptide was then aliquoted, frozen and lyophilized, and stored at −20 °C.

Monomer isolation for kinetic assays

To isolate pure monomer, Aβ peptides were subjected to size-exclusion chromatography (SEC) immediately before preparing aggregation kinetic assays. Aliquots of purified, lyophilized Aβ were dissolved in 1.0 mL 6 M GuHCl, injected on a Superdex 75 10/300 GL column, and eluted with an isocratic 0.7 mL min^{-1} flow of 20 mM sodium phosphate buffer, pH 7.4,

with 200 μM EDTA and 0.02% NaN$_3$. Typical retention times were between 19 and 21 minutes for all peptides. The center of the monomer peak was collected on ice using low-binding Eppendorf tubes. The concentration of purified peptide was determined by integrating the absorbance at 280 nm of the collected peak, using $\varepsilon_{280} = 1400$ L mol^{-1} cm^{-1} (based on the presence of a single tyrosine residue in each alloform). Concentration determination in this manner is accurate within ±20%.

Preparation of unseeded kinetic assays for pure peptides

A dilution series was prepared from the SEC-purified peptide. First, thioflavin T (ThT, Calbiochem) was added to the sample from a concentrated stock solution (filtered through 0.2 μm filter) to a final concentration of 20 μM. The dilution series was then prepared from this peptide solution, using 20 mM sodium phosphate buffer, pH 7.4, with 200 μM EDTA, 0.02% NaN$_3$, and 20 μM ThT (at this concentration, ThT fluorescence was found to scale linearly with aggregate concentration for all alloforms, Fig. S5†). All samples were prepared in low-binding tubes on ice (Axygen). The samples were loaded from low to high peptide concentration, with five wells per sample and 90 μL per well, into a 96-well, half-area, clear bottomed, PEG-coated, black polystyrene plate (Corning 3881), which was subsequently sealed. The whole setup was repeated at least three times for each peptide.

Preparation of multimolecular unseeded kinetic assays

All four peptides were purified separately by SEC, as described above. ThT was added from a concentrated stock solution to each of the purified peptides to a final concentration of 20 μM. Additionally, a dilution solution of 20 mM sodium phosphate buffer, pH 7.4, with 200 μM EDTA, 0.02% NaN$_3$, and 20 μM ThT was prepared. The purified peptide solutions and the dilution solution were combined in varying quantities to give the desired molar ratios and total concentrations. The samples were then loaded from low to high concentration of the most aggregation-prone peptide in the mixture, with four to five 90 μL wells per sample, into a 96-well plate (Corning 3881), which was subsequently sealed. The whole setup was repeated at least three times for each peptide combination.

Preparation of self- and cross-seeded kinetic assays

Seed fibrils were made from SEC-purified peptide, with fibril formation monitored by ThT fluorescence, as described above. Seed fibrils were removed once the fluorescence plateau was reached, approximately 20 hours for $A\beta_{37}$, 48 hours for $A\beta_{38}$, 5 hours for $A\beta_{40}$, and 1 hour for $A\beta_{42}$. These seed fibrils were then added in varying concentrations to aliquots of a solution of SEC-purified monomeric peptide, to which ThT had been added to a final concentration of 20 μM. For all seeded experiments, the aggregation of a set of unseeded control samples was run in parallel to the seeded reactions. Four technical replicates of each sample were then plated into a 96-well plate (Corning 3881). The whole setup was repeated at least twice for each peptide combination.

Kinetic assays

ThT fluorescence was measured using a FLUOstar Omega or FLUOstar Optima plate reader (BMG Labtech) at 37 °C under quiescent conditions. Fluorescence was measured through the bottom of the plate using an excitation filter of 440 nm and an emission filter of 480 nm, with measurements taken every 60–120 s (depending on the aggregation propensity of the alloform being studied).

Kinetic analysis

All kinetic analyses were performed using the free online program AmyloFit (www.amylofit.ch.cam.ac.uk).[59] To facilitate half-time determination and fitting of various mechanistic models, fluorescence data were normalized, using both a zero-point offset (in case of seeded experiments) and end-point normalization. For data sets with multiple fluorescence transitions, only the first transition, corresponding to $A\beta_{42}$ aggregation, was normalized; for this, the intermediate plateau phase was used as the aggregation endpoint.

Aggregation half-times were determined by performing a linear fit to the normalized ThT fluorescence data for the period in which the signal intensity was between 0.4 and 0.6. The half-time was taken to be the time at which the linear fit equals 0.5. When applicable, the scaling exponent was determined by plotting the half-time versus the relevant starting monomer concentration and fitting to this data a power function

$$t_{1/2} = \alpha[m]_0^\gamma$$

where $t_{1/2}$ is the half-time, $[m]_0$ is the starting monomer concentration, α is a proportionality constant, and γ is the scaling exponent.

The fitting of mechanistic models was used to assess which of the microscopic $A\beta_{42}$ aggregation steps are perturbed in $A\beta_{42}/A\beta_{38}$ and $A\beta_{42}/A\beta_{37}$ binary mixtures. For this, the data from the sample containing only $A\beta_{42}$ was fitted first, using the integrated rate law

$$\frac{[M]}{[M]_\infty} = 1 - \left(1 - \frac{[M]_0}{[M]_0}\right)e^{-k_\infty t} \times \left(\frac{B_- + C_+ e^{\kappa t}}{B_+ + C_+ e^{\kappa t}} \times \frac{B_+ + C_+}{B_- + C_+}\right)^{\frac{k_\infty^2}{\kappa \overline{k}_\infty}}$$

for which the parameters are defined

$$\kappa = \sqrt{2[m]_0 k_+ \frac{[m]_0^{n_2} k_2}{1 + [m]_0^{n_2}/K_M}}$$

$$\lambda = \sqrt{2k_+ k_n [m]_0^{n_c}}$$

$$C_\pm = \frac{k_+[P]_0}{\kappa} \pm \frac{k_+[M]_0}{2[m]_0 k_+} \pm \frac{\lambda^2}{2\kappa^2}$$

$$k_\infty = 2k_+[P]_\infty$$

$$\overline{k}_\infty = \sqrt{k_\infty^2 - 2C_+ C_- \kappa^2}$$

$$B_\pm = \frac{k_\infty \pm \overline{k}_\infty}{2\kappa}$$

were $[m]_0$ is the initial monomer concentration; $[P]_0$ is the fibril number at the start of the reaction; $[P]_\infty$ is the fibril number at equilibrium, when the reaction has reached completion (see ref. 38 for the detailed expression of $[P]_\infty$); $[M]_0$ is the fibril mass concentration at the start of the reaction; $[M]_\infty$ is the fibril mass concentration at equilibrium; k_n, k_2, and k_+ are the rate constants for primary nucleation, secondary nucleation, and elongation, respectively; K_M is the saturation constant for secondary nucleation; and n_c and n_2 are the reaction orders of primary and secondary nucleation, respectively.

For this fitting, the primary and secondary nucleation reaction orders (n_c and n_2, respectively) both set to 2, based on previously reported data for $A\beta_{42}$ under similar conditions,[37,41] and the initial seed concentration was set to 0. The rate constants k_+, k_n, and k_2 (corresponding to elongation, primary nucleation, and secondary nucleation, respectively) were simultaneously fitted to the data, thus accounting for any minor differences in the starting monomer concentration. For the analysis of each binary aggregation data set, three different fits were performed with one rate constant as a variable parameter and the other two rate constants fixed to the values obtained for Ab_{42} alone. The comparison of the three fits reveals whether selective perturbation of a given process could accurately model the observed inhibition of $A\beta_{42}$ aggregation.

Monomer depletion by HPLC

The samples used for monomer depletion studies were prepared and incubated as described above, with aggregation monitored by ThT fluorescence. All samples were prepared to a concentration of 3 μM each $A\beta_{42}$, $A\beta_{40}$, and either $A\beta_{38}$ or $A\beta_{37}$ and plated in 100 μL aliquots. One sample was removed into a low-binding tube (Axygen) at the start of incubation, with additional samples removed during the initial lag phase, the first fluorescence transition, the intermediate plateau phase, the second fluorescence transition, and the final plateau phase. In addition to the removed samples, two additional samples were left in the plate to monitor the entire aggregation process.

Upon removal, each sample was centrifuged at 20 000 × g for 5 min at room temperature to sediment the aggregated peptide. Following centrifugation, the upper 50 μL of the supernatant was removed and injected on an analytical HPLC instrument (Agilent 1100), equipped with a C8 column (Agilent ZORBAX 300SB, 200 × 4.6 mm), run at a flow rate of 1 mL min^{-1} at 70 °C. The mobile phases used were (solvent A) 0.1% formic acid in water and (solvent B) 0.1% formic acid in acetonitrile. A linear gradient of 15–30% B over 10 min, followed by an isocratic flow of 30% B for an additional five min was used. The

approximate retention times for each peptide were as follows: $A\beta_{42} = 13.7$ min, $A\beta_{40} = 12.0$ min, $A\beta_{38} = 10.6$ min, $A\beta_{37} = 10.8$ min.

Fibril composition by HPLC

Samples were prepared and incubated as described above, with aggregation monitored by ThT fluorescence. All samples were prepared to a concentration of 3 μM each of $A\beta_{42}$, $A\beta_{40}$, and either $A\beta_{38}$ or $A\beta_{37}$, and plated in 125 μL aliquots. Samples were removed at the start of incubation, during the intermediate plateau phase, and the final plateau phase. At each time point, the contents of two wells were removed and combined to give a total sample volume of 250 μL. In addition to the removed samples, two additional samples were left in the plate to monitor the aggregation process.

Upon removal, samples were filtrated through 0.2 μm spin filters (VIVASPIN 500) at $15\,000 \times g$ for 5 min at room temperature to trap the fibrils. The filter-trapped fibrils were then washed five times with 500 μL ultrapure water (to a total wash volume of 10x the sample volume) to remove any monomeric or oligomeric peptide on the fibril and filter surface. After each wash, the sample was centrifuged at $15\,000 \times g$ for 5 min at room temperature, leaving a retentate volume of ca. 25 μL. After the final wash, the retentate was mixed in a 1 : 3 ratio with 6 M GuHCl to dissolve the fibrils for 15 min before being injected on an analytical HPLC instrument. HPLC was performed as described above.

Cryo-EM

For Cryo-EM samples, monomer isolation for all peptides was performed as described above. Solutions were prepared with a total monomeric peptide concentration of 10 μM and incubated in the same manner as for the kinetic assays, with aggregation monitored by ThT fluorescence. Samples were taken once the final fluorescence plateau was reached. Specimens were prepared for imaging in a controlled environment vitrification system (CEVS) to maintain stable temperature and to minimize solution loss. The sample was prepared as a thin liquid film, <300 nm thick, on lacey carbon filmed copper grids. This was plunged into liquid ethane at -180 °C to vitrify the sample; this minimizes water crystallization as well as component segmentation and rearrangement, thus maintaining original microstructures. The vitrified sample was stored under liquid nitrogen until imaged. The grid was transferred into the electron microscope (JEM 2200FS) using a Fischione Model 2550 cryo transfer tomography holder. The microscope was equipped with an in-column energy filter (Omega filter), thus allowing for zero-loss imaging. The acceleration voltage was 200 kV and zero-loss images were recorded digitally with a TVIPS F416 camera using SerialEM under low dose conditions and with a 30 eV energy selecting slit in place.

To quantify fibril ultrastructure, the node-to-node distance and fibril diameter were measured using ImageJ (version 2.1.0/1.53c, NIH). For each sample, at least 50 measurements were performed, measuring at least fifteen total fibrils from five different images, each taken from different parts of the sample grid. Measurements are presented in boxplots with Tukey whiskers, with the median represented by the center line, the box containing the 25th–75th percentiles, and individually plotted points representing statistical outliers. Statistical significance was assessed using a one-way ANOVA followed by Dunnett's post-hoc test, with $p < 0.05$ considered significant. All statistical analysis was performed in GraphPad Prism (version 9.0.2).

Data availability

All data presented in this article will be made available upon reasonable request.

Author contributions

H. Z. and S. L. designed the study. G. A. B., K. S. and S. L. performed the experiments. G. A. B. and A. J. D. analyzed data. G. A. B. wrote the paper with input from all co-authors.

Conflicts of interest

H. Z. has served at scientific advisory boards for Eisai, Denali, Roche Diagnostics, Wave, Samumed, Siemens Healthineers, Pinteon Therapeutics, Nervgen, AZTherapies and CogRx, has given lectures in symposia sponsored by Cellectricon, Fujirebio, Alzecure and Biogen, and is a co-founder of Brain Biomarker Solutions in Gothenburg AB (BBS), which is a part of the GU Ventures Incubator Program (outside submitted work).

Acknowledgements

References

1 C. A. Lane, J. Hardy and J. M. Schott, *Eur. J. Neurol.*, 2018, **25**, 59–70.

2 *Developing therapeutics for Alzheimer's disease: progress and challenges*, ed., M. S. Wolfe, Elsevier/AP, Academic Press is an imprint of Elsevier, Amsterdam; Boston, 2016.

3 A. B. Reiss, H. A. Arain, M. M. Stecker, N. M. Siegart and L. J. Kasselman, *Rev. Neurosci.*, 2018, **29**, 613–627.

4 J. L. Cummings, G. Tong and C. Ballard, *J. Alzheimer's Dis.*, 2019, **67**, 779–794.

5 J. Sevigny, P. Chiao, T. Bussière, P. H. Weinreb, L. Williams, M. Maier, R. Dunstan, S. Salloway, T. Chen, Y. Ling, J. O'Gorman, F. Qian, M. Arastu, M. Li, S. Chollate, M. S. Brennan, O. Quintero-Monzon, R. H. Scannevin,

H. M. Arnold, T. Engber, K. Rhodes, J. Ferrero, Y. Hang, A. Mikulskis, J. Grimm, C. Hock, R. M. Nitsch and A. Sandrock, *Nature*, 2016, **537**, 50–56.

6 S. B. Haeberlein, *Presented in part at the 12th Clinical Trials on Alzheimer's Disease (CTAD) Congress*, San Diego, CA, 2019.

7 S. Linse, T. Scheidt, K. Bernfur, M. Vendruscolo, C. M. Dobson, S. I. A. Cohen, E. Sileikis, M. Lundqvist, F. Qian, T. O'Malley, T. Bussiere, P. H. Weinreb, C. K. Xu, G. Meisl, S. R. A. Devenish, T. P. J. Knowles and O. Hansson, *Nat. Struct. Mol. Biol.*, 2020, **27**, 1125–1133.

8 *"FDA Grants Accelerated Approval for Alzheimer's Drug."* June 2021. https://www.fda.gov/news-events/press-announcements/fda-grants-accelerated-approval-alzheimers-drug. Accessed October 2021.

9 J. Hardy and D. Allsop, *Trends Pharmacol. Sci.*, 1991, **12**, 383–388.

10 J. Hardy and G. Higgins, *Science*, 1992, **256**, 184–185.

11 E. N. Cline, M. A. Bicca, K. L. Viola and W. L. Klein, *J. Alzheimer's Dis.*, 2018, **64**, S567–S610.

12 M. G. Iadanza, M. P. Jackson, E. W. Hewitt, N. A. Ranson and S. E. Radford, *Nat. Rev. Mol. Cell Biol.*, 2018, **19**, 755–773.

13 S. Linse, *Biophys. Rev.*, 2017, **9**, 329–338.

14 M. Törnquist, T. C. T. Michaels, K. Sanagavarapu, X. Yang, G. Meisl, S. I. A. Cohen, T. P. J. Knowles and S. Linse, *Chem. Commun.*, 2018, **54**, 8667–8684.

15 R. M. Ransohoff, *Science*, 2016, **353**, 777–783.

16 V. Calsolaro and P. Edison, *Alzheimer's Dementia*, 2016, **12**, 719–732.

17 F. Kametani and M. Hasegawa, *Front. Neurosci.*, 2018, **12**, 25.

18 G. S. Bloom, *JAMA Neurol.*, 2014, **71**, 505.

19 G. K. Gouras, T. T. Olsson and O. Hansson, *Neurotherapeutics*, 2015, **12**, 3–11.

20 D. J. Selkoe and J. Hardy, *EMBO Mol. Med.*, 2016, **8**, 595–608.

21 P. Arosio, M. Vendruscolo, C. M. Dobson and T. P. J. Knowles, *Trends Pharmacol. Sci.*, 2014, **35**, 127–135.

22 Y. Zhang, R. Thompson, H. Zhang and H. Xu, *Mol. Brain*, 2011, **4**, 3.

23 C. Haass, C. Kaether, G. Thinakaran and S. Sisodia, *Cold Spring Harbor Perspect. Med.*, 2012, **2**, a006270.

24 K. G. Mawuenyega, T. Kasten, W. Sigurdson and R. J. Bateman, *Anal. Biochem.*, 2013, **440**, 56–62.

25 N. Kaneko, R. Yamamoto, T.-A. Sato and K. Tanaka, *Proc. Jpn. Acad., Ser. B*, 2014, **90**, 104–117.

26 J. Reinert, B. C. Richard, H. W. Klafki, B. Friedrich, T. A. Bayer, J. Wiltfang, G. G. Kovacs, M. Ingelsson, L. Lannfelt, A. Paetau, J. Bergquist and O. Wirths, *Acta Neuropathol. Commun.*, 2016, **4**, 24.

27 G. Brinkmalm, W. Hong, Z. Wang, W. Liu, T. T. O'Malley, X. Sun, M. P. Frosch, D. J. Selkoe, E. Portelius, H. Zetterberg, K. Blennow and D. M. Walsh, *Brain*, 2019, **142**, 1441–1457.

28 M. Bibl, B. Mollenhauer, H. Esselmann, P. Lewczuk, H.-W. Klafki, K. Sparbier, A. Smirnov, L. Cepek, C. Trenkwalder, E. Rüther, J. Kornhuber, M. Otto and J. Wiltfang, *Brain*, 2006, **129**, 1177–1187.

29 J. Wiltfang, H. Esselmann, M. Bibl, A. Smirnov, M. Otto, S. Paul, B. Schmidt, H.-W. Klafki, M. Maler, T. Dyrks, M. Bienert, M. Beyermann, E. Rüther and J. Kornhuber, *J. Neurochem.*, 2002, **81**, 481–496.

30 D. Galasko, L. Chang, R. Motter, C. M. Clark, J. Kaye, D. Knopman, R. Thomas, D. Kholodenko, D. Schenk, I. Lieberburg, B. Miller, R. Green, R. Basherad, L. Kertiles, M. A. Boss and P. Seubert, *Arch. Neurol.*, 1998, **55**, 937.

31 P. E. Spies, M. M. Verbeek, T. van Groen and J. A. H. R. Claassen, *Front. Biosci., Landmark Ed.*, 2012, **17**, 2024–2034.

32 S. Zampar, H. W. Klafki, K. Sritharen, T. A. Bayer, J. Wiltfang, A. Rostagno, J. Ghiso, L. A. Miles and O. Wirths, *Neuropathol. Appl. Neurobiol.*, 2020, **46**, 673–685.

33 O. Szczepankiewicz, B. Linse, G. Meisl, E. Thulin, B. Frohm, C. Sala Frigerio, M. T. Colvin, A. C. Jacavone, R. G. Griffin, T. Knowles, D. M. Walsh and S. Linse, *J. Am. Chem. Soc.*, 2015, **137**, 14673–14685.

34 T. Weiffert, G. Meisl, P. Flagmeier, S. De, C. J. R. Dunning, B. Frohm, H. Zetterberg, K. Blennow, E. Portelius, D. Klenerman, C. M. Dobson, T. P. J. Knowles and S. Linse, *ACS Chem. Neurosci.*, 2019, **10**, 2374–2384.

35 M. P. Murphy and H. LeVine, *J. Alzheimer's Dis.*, 2010, **19**, 311–323.

36 A. Vandersteen, E. Hubin, R. Sarroukh, G. De Baets, J. Schymkowitz, F. Rousseau, V. Subramaniam, V. Raussens, H. Wenschuh, D. Wildemann and K. Broersen, *FEBS Lett.*, 2012, **586**, 4088–4093.

37 S. I. A. Cohen, S. Linse, L. M. Luheshi, E. Hellstrand, D. A. White, L. Rajah, D. E. Otzen, M. Vendruscolo, C. M. Dobson and T. P. J. Knowles, *Proc. Natl. Acad. Sci. U. S. A.*, 2013, **110**, 9758–9763.

38 G. Meisl, X. Yang, E. Hellstrand, B. Frohm, J. B. Kirkegaard, S. I. A. Cohen, C. M. Dobson, S. Linse and T. P. J. Knowles, *Proc. Natl. Acad. Sci. U. S. A.*, 2014, **111**, 9384–9389.

39 A. Abelein, J. Jarvet, A. Barth, A. Gräslund and J. Danielsson, *J. Am. Chem. Soc.*, 2016, **138**, 6893–6902.

40 G. Meisl, X. Yang, C. M. Dobson, S. Linse and T. P. J. Knowles, *Chem. Sci.*, 2017, **8**, 4352–4362.

41 G. Meisl, X. Yang, B. Frohm, T. P. J. Knowles and S. Linse, *Sci. Rep.*, 2016, **6**, 18728.

42 R. Sabaté, A. Espargaró, L. Barbosa-Barros, S. Ventura and J. Estelrich, *Biochimie*, 2012, **94**, 1730–1738.

43 A. K. Srivastava, J. M. Pittman, J. Zerweck, B. S. Venkata, P. C. Moore, J. R. Sachleben and S. C. Meredith, *Protein Sci.*, 2019, **28**, 1567–1581.

44 C. Cabaleiro-Lago, F. Quinlan-Pluck, I. Lynch, S. Lindman, A. M. Minogue, E. Thulin, D. M. Walsh, K. A. Dawson and S. Linse, *J. Am. Chem. Soc.*, 2008, **130**, 15437–15443.

45 K. Ezzat, M. Pernemalm, S. Pålsson, T. C. Roberts, P. Järver, A. Dondalska, B. Bestas, M. J. Sobkowiak, B. Levänen, M. Sköld, E. A. Thompson, O. Saher, O. K. Kari, T. Lajunen, E. Sverremark Ekström, C. Nilsson, Y. Ishchenko, T. Malm, M. J. A. Wood, U. F. Power, S. Masich, A. Lindén, J. K. Sandberg, J. Lehtiö, A.-L. Spetz and S. EL Andaloussi, *Nat. Commun.*, 2019, **10**, 2331.

46 E. R. Padayachee, H. Zetterberg, E. Portelius, J. Borén, J. L. Molinuevo, N. Andreasen, R. Cukalevski, S. Linse,

K. Blennow and U. Andreasson, *Brain Res.*, 2016, **1651**, 11–16.

47 R. Frankel, M. Törnquist, G. Meisl, O. Hansson, U. Andreasson, H. Zetterberg, K. Blennow, B. Frohm, T. Cedervall, T. P. J. Knowles, T. Leiding and S. Linse, *Commun. Biol.*, 2019, **2**, 365.

48 R. Cukalevski, X. Yang, G. Meisl, U. Weininger, K. Bernfur, B. Frohm, T. P. J. Knowles and S. Linse, *Chem. Sci.*, 2015, **6**, 4215–4233.

49 B. D. Moore, J. Martin, L. de Mena, J. Sanchez, P. E. Cruz, C. Ceballos-Diaz, T. B. Ladd, Y. Ran, Y. Levites, T. L. Kukar, J. J. Kurian, R. McKenna, E. H. Koo, D. R. Borchelt, C. Janus, D. Rincon-Limas, P. Fernandez-Funez and T. E. Golde, *J. Exp. Med.*, 2018, **215**, 283–301.

50 M. O. Quartey, J. N. K. Nyarko, J. M. Maley, J. R. Barnes, M. A. C. Bolanos, R. M. Heistad, K. J. Knudsen, P. R. Pennington, J. Buttigieg, C. E. De Carvalho, S. C. Leary, M. P. Parsons and D. D. Mousseau, *Sci. Rep.*, 2021, **11**, 431.

51 E. Portelius, U. Andreasson, J. M. Ringman, K. Buerger, J. Daborg, P. Buchhave, O. Hansson, A. Harmsen, M. K. Gustavsson, E. Hanse, D. Galasko, H. Hampel, K. Blennow and H. Zetterberg, *Mol. Neurodegener.*, 2010, **5**, 2.

52 E. Portelius, B. Van Broeck, U. Andreasson, M. K. Gustavsson, M. Mercken, H. Zetterberg, H. Borghys and K. Blennow, *J. Alzheimer's Dis.*, 2010, **21**, 1005–1012.

53 T. C. T. Michaels, A. Šarić, S. Curk, K. Bernfur, P. Arosio, G. Meisl, A. J. Dear, S. I. A. Cohen, C. M. Dobson, M. Vendruscolo, S. Linse and T. P. J. Knowles, *Nat. Chem.*, 2020, **12**, 445–451.

54 A. Jan, O. Gokce, R. Luthi-Carter and H. A. Lashuel, *J. Biol. Chem.*, 2008, **283**, 28176–28189.

55 M. M. Murray, S. L. Bernstein, V. Nyugen, M. M. Condron, D. B. Teplow and M. T. Bowers, *J. Am. Chem. Soc.*, 2009, **131**, 6316–6317.

56 S. G. Bolder, L. M. C. Sagis, P. Venema and E. van der Linden, *Langmuir*, 2007, **23**, 4144–4147.

57 R. Silvers, M. T. Colvin, K. K. Frederick, A. C. Jacavone, S. Lindquist, S. Linse and R. G. Griffin, *Biochemistry*, 2017, **56**, 4850–4859.

58 D. M. Walsh, E. Thulin, A. M. Minogue, N. Gustavsson, E. Pang, D. B. Teplow and S. Linse, *FEBS J.*, 2009, **276**, 1266–1281.

59 G. Meisl, J. B. Kirkegaard, P. Arosio, T. C. T. Michaels, M. Vendruscolo, C. M. Dobson, S. Linse and T. P. J. Knowles, *Nat. Protoc.*, 2016, **11**, 252–272.

60 G. Meisl, T. C. T. Michaels, S. Linse and T. P. J. Knowles, in *Amyloid Proteins*, ed. E. M. Sigurdsson, M. Calero and M. Gasset, Springer New York, New York, NY, 2018, vol. 1779, pp. 181–196.

61 G. Meisl, L. Rajah, S. A. I. Cohen, M. Pfammatter, A. Šarić, E. Hellstrand, A. K. Buell, A. Aguzzi, S. Linse, M. Vendruscolo, C. M. Dobson and T. P. J. Knowles, *Chem. Sci.*, 2017, **8**, 7087–7097.

62 A. J. Dear, G. Meisl, T. C. T. Michaels, M. R. Zimmermann, S. Linse and T. P. J. Knowles, *J. Chem. Phys.*, 2020, **152**, 045101.

63 A. Munke, J. Persson, T. Weiffert, E. De Genst, G. Meisl, P. Arosio, A. Carnerup, C. M. Dobson, M. Vendruscolo, T. P. J. Knowles and S. Linse, *Proc. Natl. Acad. Sci. U. S. A.*, 2017, **114**, 6444–6449.

64 C. J. Sarell, P. G. Stockley and S. E. Radford, *Prion*, 2013, **7**, 359–368.

65 M. I. Ivanova, Y. Lin, Y.-H. Lee, J. Zheng and A. Ramamoorthy, *Biophys. Chem.*, 2021, **269**, 106507.

66 S. Chia, P. Flagmeier, J. Habchi, V. Lattanzi, S. Linse, C. M. Dobson, T. P. J. Knowles and M. Vendruscolo, *Proc. Natl. Acad. Sci. U. S. A.*, 2017, **114**, 8005–8010.

67 S. Bondarev, K. Antonets, A. Kajava, A. Nizhnikov and G. Zhouravleva, *Int. J. Mol. Sci.*, 2018, **19**, 2292.

68 F. Hasecke, C. Niyangoda, G. Borjas, J. Pan, G. Matthews, M. Muschol and W. Hoyer, *Angew. Chem., Int. Ed.*, 2021, **60**, 3016–3021.

69 J. C. Kessler, J.-C. Rochet and P. T. Lansbury, *Biochemistry*, 2003, **42**, 672–678.

70 S. Abeln and D. Frenkel, *PLoS Comput. Biol.*, 2008, **4**, e1000241.

71 C. Arber, J. Toombs, C. Lovejoy, N. S. Ryan, R. W. Paterson, N. Willumsen, E. Gkanatsiou, E. Portelius, K. Blennow, A. Heslegrave, J. M. Schott, J. Hardy, T. Lashley, N. C. Fox, H. Zetterberg and S. Wray, *Mol. Psychiatry*, 2020, **25**, 2919–2931.

72 S. Mekala, G. Nelson and Y.-M. Li, *RSC Med. Chem.*, 2020, **11**, 1003–1022.

73 M. S. Wolfe, *Molecules*, 2021, **26**, 388.

74 G. Yang, R. Zhou, X. Guo, C. Yan, J. Lei and Y. Shi, *Cell*, 2021, **184**, 521–533.e14.